frontiers in Materials

ORIGINAL RESEARCH
published: 24 July 2019
doi: 10.3389/fmats.2019.00176

Controlled Synthesis of $Ni_xCo_yS_4$/rGO Composites for Constructing High-Performance Asymmetric Supercapacitor

*Mingxia Dong, Zhixing Wang, Jiexi Wang, Huajun Guo, Xinhai Li and Guochun Yan**

School of Metallurgy and Environment, Central South University, Changsha, China

Nickel-cobalt sulfides ($Ni_xCo_yS_4$) are promising supercapacitor materials due to their high capacitance, while the sluggish kinetics in terms of charge transfer limits their energy density. To achieve both high energy and power density for the $Ni_xCo_yS_4$–based supercapacitor, sulfur-doped reduced graphene oxide (rGO) is incorporated into $Ni_xCo_yS_4$ by an *in situ* growth—ion exchange strategy to synthesize $Ni_xCo_yS_4$/rGO composites. Profited from the synergetic effect between rGO and $Ni_xCo_yS_4$, the $Ni_{1.64}Co_{2.40}S_4$/rGO electrode delivers high specific capacitance of 1,089 F g^{-1} at 1 A g^{-1}, and remains 92.6% of its original capacitance at 20 A g^{-1} (1,008 F g^{-1}). Asymmetric supercapacitors assembled with active carbon (AC) and $Ni_{1.64}Co_{2.40}S_4$/rGO ($Ni_{1.64}Co_{2.40}S_4$/rGO//AC) offer both high specific capacitance (265.5 F g^{-1} at 1 A g^{-1}) and superior rate capability at 50 A g^{-1} (recovering 63.6% of the capacitance determined at 1 A g^{-1}). In addition, the assembled device exhibits a high capacitance retention of 92.6% after 10,000 cycles at 10 A g^{-1}, which implies an excellent cyclic stability. Ragone plot reveals that the energy density of $Ni_{1.64}Co_{2.40}S_4$/rGO//AC asymmetric supercapacitor do not vanish as it delivers 30.4 Wh kg^{-1} at 10 kW kg^{-1}, demonstrating its promising application.

Keywords: nickel-cobalt sulfides, *in-situ* growth, high energy density, asymmetric supercapacitor, high cyclic stability

OPEN ACCESS

Edited by:
Shengkui Zhong,
Soochow University, China

Reviewed by:
Biao Gao,
Wuhan University of Science and Technology, China
Chaopeng Fu,
Shanghai Jiao Tong University, China

****Correspondence:***
Guochun Yan
happyygc@csu.edu.cn

Specialty section:
This article was submitted to Energy Materials, a section of the journal Frontiers in Materials

Received: *29 May 2019*
Accepted: *08 July 2019*
Published: *24 July 2019*

Citation:
Dong M, Wang Z, Wang J, Guo H, Li X and Yan G (2019) Controlled Synthesis of $Ni_xCo_yS_4$/rGO Composites for Constructing High-Performance Asymmetric Supercapacitor. Front. Mater. 6:176. doi: 10.3389/fmats.2019.00176

INTRODUCTION

With gradual consumption of fuel energy and the growing environmental problems, is the need to develop renewable energies and corresponding energy storage and conversion devices is urgent (Zhong et al., 2012; Liu et al., 2018a; Zhang Q. et al., 2018). Lithium ion battery (Li et al., 2015; Liu et al., 2016; Zhong et al., 2017; Wang J. et al., 2018), sodium-ion battery (Chen J. et al., 2018; Yan et al., 2018), Lithium-Sulfur battery (Tan et al., 2018; Wu F. et al., 2018), and supercapacitor (Gilshteyn et al., 2017; Saha et al., 2018) are representative electrochemical energy storage devices. A supercapacitor (SC) is one of the most promising energy storage devices due to their desirable characteristics, such as high power-density, super-long cycle life and high safety performance, and it plays an important role in both automobile and electronic industry (Simon et al., 2014; Eftekhari et al., 2017; Zhang L. et al., 2018). Classified by different energy storage mechanisms, electrical double layer capacitors (EDLCs), and pseudocapacitors (PCs) show differentiated advantages in the specific field. Although EDLCs deliver fast electron transfer, their

bottleneck lies in the low specific capacitance problem. On the contrary, PCs deliver satisfying specific capacitance, but poor charge transfer ability limits their application. Neither of them can be used to build a capacitor that possesses both high energy density and power density. Developing a hybrid capacitor combining with the advantages of EDLCs and PCs is an effective strategy to remedy the deficiency.

To fulfill the above design, developing advanced materials with both high capacitance and rate capability are the key factors. Normally, the composite formed with proper composition of two materials results in complementary advantages. As known to all, reduced graphene oxide (rGO) is one of the most promising electrode materials for EDLCs due to its large specific surface area, exceptionally high electronic conductivity and high theoretical specific capacitance (Booth et al., 2008; Lee et al., 2008; Ke and Wang, 2016). When rGO is introduced into the composite properly, it enhances not only the electronic conductivity of composite, but also the structural stability of the electrode (Ke and Wang, 2016; Deng et al., 2017). Therefore, taking reduced graphene oxide as a framework is an effective way to reinforce the mechanical strengths of the composites. Nickel-cobalt sulfide is one of the most promising one among various pseudocapacitor electrode materials, such as metal oxides, metal sulfides, and conductive polymers (Jinlong et al., 2017; Wen et al., 2017; Zhao et al., 2017; Liang et al., 2018). Although, there is some doubt about the definition of pseudocapacitance (Brousse, 2015; Jiang and Liu, 2019), many studies reported that transition metal sulfides were classified as one kind of pseudocapacitive materials (Xiong et al., 2015; Wang et al., 2019). However, some studies classify transition metal sulfides as battery-type electrode materials (Mohamed et al., 2018; Ma et al., 2019). Putting this controversial issue aside, it has been proven that nickel-cobalt sulfides ($Ni_xCo_yS_4$) exhibit high electronic conductivity and flexibility due to the lower optical band gap of Ni–Co and electronegativity of sulfur (Chen et al., 2013; Zhu et al., 2015). Great efforts have been devoted to the fabrication of composites, such as $NiCo_2S_4$/rGO (Annamalai et al., 2017; Nan et al., 2018; Sarkar et al., 2018; Wang Y. et al., 2018), $CoNi_2S_4$/rGO (Gao et al., 2018), NiS/rGO (Qu et al., 2018), C-$NiCo_2S_4$ (Yuan et al., 2017; Mohamed et al., 2018), CNTs-$NiCo_2S_4$ (Li D. et al., 2016), and so on. However, the influence of Ni/Co ratio of nickel-cobalt sulfide materials on the characteristics and the pseudocapacitance performances are not systematically studied.

In this work, we prepare a series of $Ni_xCo_yS_4$/rGO composites with various Ni/Co ratios in the raw materials (Ni/Co = 2.0, 1.0, 0.5, and 0.25), in which the bimetallic Ni-Co hydroxy-carbonates *in-situ* grow onto the rGO framework during the synthesis process. We demonstrate that asymmetric supercapacitor ($Ni_{1.64}Co_{2.40}S_4$/rGO//AC) assembled with $Ni_{1.64}Co_{2.40}S_4$/rGO composite (positive electrode) and active carbon (negative electrode) exhibits excellent electrochemical performance with outstanding capacitance retention of 92.6% after 10,000 cycles at high current density of 10 A g^{-1} and high energy density of 30.4 Wh kg^{-1} at the power density of 10 kW kg^{-1}. Our results offer new insights into developing advanced electrode materials for supercapacitors with high energy and power density.

EXPERIMENTAL

The graphene oxide (GO) was purchased from Suzhou Tanfeng technology co LTD, and all of other chemical reagents were provided by Sinopharm Chemical Reagent Corp in an analytical grade that were used as-received without further purification.

Synthesis of $Ni_xCo_yS_4$

In a typical synthesis of precursors, 0.025 g GO was dissolved into 100 mL deionized water to form homogeneous brown solution by ultrasonic dispersion. A certain mass of $NiCl_2{\cdot}6H_2O$, $CoCl_2{\cdot}6H_2O$ (molar ratios of Ni: Co are 2:1, 1:1; 1:2, and 1:4) and 1.6365 g urea were dissolved into the GO solution under stirring. After stirring for 30 min, the obtained suspension was transferred into a 200 mL Teflon-lined autoclave. The hydrothermal reaction was carried out at 120°C for 10 h so that the bimetallic Ni-Co hydroxy-carbonates *in-situ* grow onto the GO framework. The products were washed with deionized water and collected through filtration, and then which was lyophilized. Based on the Ni/Co ratio in the raw materials, the as-obtained precursors were labeled as NC2010, NC1515, NC1020, and NC0624, respectively.

For synthesizing the $Ni_xCo_yS_4$/rGO by sulfurizing the aforementioned precursors, the representative processes are described as followed. First, 0.2 g precursor was dispersed into 100 mL deionized water and the mixture was stirred for 30 min. Subsequently, 1.7156 g $Na_2S{\cdot}9H_2O$ was added into the suspension and stirred for 30 min. Then, the mixture was transferred into a 200 mL Teflon-lined autoclave, which was heated at 180°C for 8 h. After cooling naturally to room temperature, the black product was collected in the same way as former procedure. To further illuminate the content of Ni, Co and S in the $Ni_xCo_yS_4$/rGO composites, the Inductively Coupled Plasma-Optical Emission Spectrometry (ICP-OES) results and the C-S analysis results of $Ni_xCo_yS_4$/rGO composites are shown in **Table S1**. The as-prepared products were labeled as $Ni_{2.15}Co_{1.37}S_4$/rGO, $Ni_{1.64}Co_{2.40}S_4$/rGO, $Ni_{1.02}Co_{2.98}S_4$/rGO, $Ni_{0.60}Co_{3.60}S_4$/rGO on the basis of ICP and C-S analysis results.

Materials Characterization

Structure, morphology, and microstructure of the precursors and the corresponding $Ni_xCo_yS_4$/rGO composites were characterized by X-ray diffraction using Cu Kα (λ = 1.5406 Å) radiation (XRD, Bruker D8 AdvanceRint-2000), scanning electron microscopy (SEM, Sirion 200), and transmission electron microscopy (TEM, Tecnai G12, 200 kV). The Surface elemental valence of the sample was characterized by X-ray photoelectron spectroscopy (XPS, PHI5600, PerkineElmer).

Electrochemical Measurement

Circular Ni foams were cleaned in 1.0 mol L^{-1} KOH solution with ultrasonic cleaning for 30 min to remove impurities on the surface, and washed with deionized water three times. The preparation of electrodes was followed in the same procedure as described in previous work (Dong et al., 2018), and the diameter of Ni foam for positive and negative electrode is 12 and 16 mm, respectively.

Electrochemical tests were performed in three-electrode systems with 6 mol L^{-1} KOH as electrolyte, the working electrode was prepared by mixing $Ni_xCo_yS_4$/rGO composites, conductive additive (Super P), and binder (60 wt% PTFE emulsion) in a ratio of 8:1:1, Hg/HgO electrode as the reference electrode and Pt electrode as the counter electrode, respectively. By contrast, electrochemical tests carried out in the asymmetric supercapacitor were based on the abovementioned working electrode (positive electrode) and active carbon electrode (negative electrode), in which the active carbon electrode was prepared by mixing active carbon, conductive additive (Super P) and binder (60 wt% PTFE emulsion) in a ratio of 85:10:5. Cyclic voltammetry (CV) and electrochemical impedance spectroscopy (EIS) were tested by a CHI 660D electrochemical workstation (Chenhua Instruments, Shanghai). Galvanostatic charge-discharge (GCD) tests were carried out with the LAND electrochemical test system. Additional experimental details are described in the **Supplementary Material** of the work.

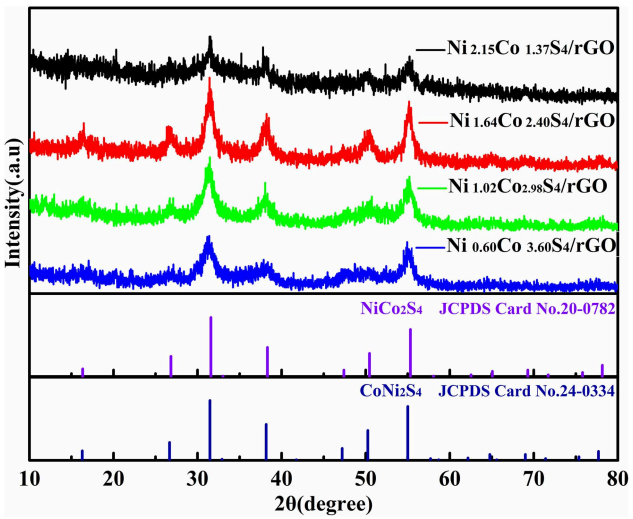

FIGURE 1 | XRD patterns of $Ni_xCo_yS_4$/rGO composites.

RESULT AND DISCUSSION

The crystallographic characteristics of the as-obtained precursors and $Ni_xCo_yS_4$/rGO composites are characterized by XRD. As shown in **Figure S2**, for all samples, most of the diffraction peaks can be indexed to $Ni_xCo_y(CO_3)_{0.5}(OH)$ ($x+y=1$) that is derived from $Co(CO_3)_{0.5}(OH)\cdot 0.11H_2O$ (JCPDS Card No.48-0083). No impurity peaks were observed, which illustrates the substitution of Co by Ni during the growth of crystals with the increasing of nickel contents in the precursors (Xiao and Yang, 2011; Wan et al., 2013). With the decrease of Ni/Co ratio, the intensities of the diffraction peaks increase gradually, suggesting that the Co element plays a role in improving the crystallinity of precursor. For the XRD patterns of $Ni_xCo_yS_4$/rGO composites (**Figure 1**), all of the XRD patterns of all $Ni_xCo_yS_4$/rGO composites show weak diffraction peaks. The diffraction peaks at the 2θ of 31.4°, 38.2°, 50.1°, and 55.1° are ascribed to (311), (400), (511), and (440) planes of the cubic $NiCo_2S_4$ (JCPDS Card No.20-0782) or $CoNi_2S_4$ (JCPDS Card No.24-0334). The $Ni_{1.64}Co_{2.40}S_4$/rGO composite owns the strongest diffraction peaks, reflecting the highest crystallinity among all samples.

SEM and TEM technique were used to characterize the morphology of the precursors and $Ni_xCo_yS_4$/rGO composites as shown in **Figures S3, S4** and **Figure 2**. **Figures S3a–d** show SEM images and EDS results of NC2010, NC1515, NC1020, and NC0624, respectively. For all precursors, a nano-needle type of Ni-Co compounds were embedded onto the surface of rGO network. With the decrease of Ni/Co ratio, the size of nano-needles gradually increases as shown in **Figure S3**. The NC0624 possess maximum microscopic size with a longitudinal length larger than 2 μm, indicating that Co plays a crucial role in the vertical growth of crystal. EDS results reveals that the ratio of Ni/Co content decrease from 1.5 to 0.2, which is in well-accordance with our experimental design. Furthermore, the TEM and high-resolution transmission electron microscope (HRTEM) images of NC1515 are carried out to further illustrate the morphology and microstructure of the precursor. As shown in **Figure S4**, the Ni-Co compounds with solid nano-needle morphology evenly distributed on the surface of rGO with transparent morphology, and the diameter of the nanoneedle is about 20 nm. The interplanar crystal spacing of 0.88 nm in the HRTEM image (**Figure S4d**) can be referred to the (100) plane of $Ni_xCo_y(CO_3)_{0.5}(OH)$.

Figures 2a–d show SEM images of $Ni_{2.15}Co_{1.37}S_4$/rGO, $Ni_{1.64}Co_{2.40}S_4$/rGO, $Ni_{1.02}Co_{2.98}S_4$/rGO, and $Ni_{0.60}Co_{3.60}S_4$/rGO composites, respectively. It is obvious that the sulfides inherit the morphological features of corresponding precursors with the $Ni_xCo_yS_4$ decorated on the surface of rGO. It is worth noting that the TEM images of $Ni_{1.64}Co_{2.40}S_4$/rGO (see **Figure S4** and **Figures 2e–h**) confirms that the solid nano-needles transfer to nano-tube during ion exchange process from the precursor to sulfides. Specifically, the hollow structures with a rough surface possess an outer diameter of about 35 nm, which is larger than the diameter of the precursor (20 nm). The TEM results of precursors and $Ni_{1.64}Co_{2.40}S_4$/rGO composite suggest that the Ni^{2+} ions and Co^{2+} ions diffused outwards from the precursor and combined with sulfur ions to form sulfides. The EDS results of $Ni_xCo_yS_4$/rGO composites in **Figure S1** reveals that Ni, Co, and S elements exist on the surface of the composites. In addition, it is worth noting that the S-doped graphene is also formed during the ion-exchange process, which is evidenced by a set of comparison experiments. Specifically, the GO was reduced in $Na_2S\cdot 9H_2O$ solution under the same condition as preparing $Ni_xCo_yS_4$/rGO composites, which can be confirmed by the C1s, and O1s XPS spectra in **Figure S5**. Moreover, the characteristic of sulfur peak in the EDS spectra (**Figure S6**) and C=S, C-S-C bonds in S2p spectra of aforementioned rGO sample confirm the existence of sulfur in rGO, which is beneficial to improve the pseudo-capacitance because of the heteroatom doping of S (Liu et al., 2017).

To further probe the formation of nickel-cobalt sulfides ($Ni_xCo_yS_4$) and the S-doped rGO in the sulfide composite, XPS

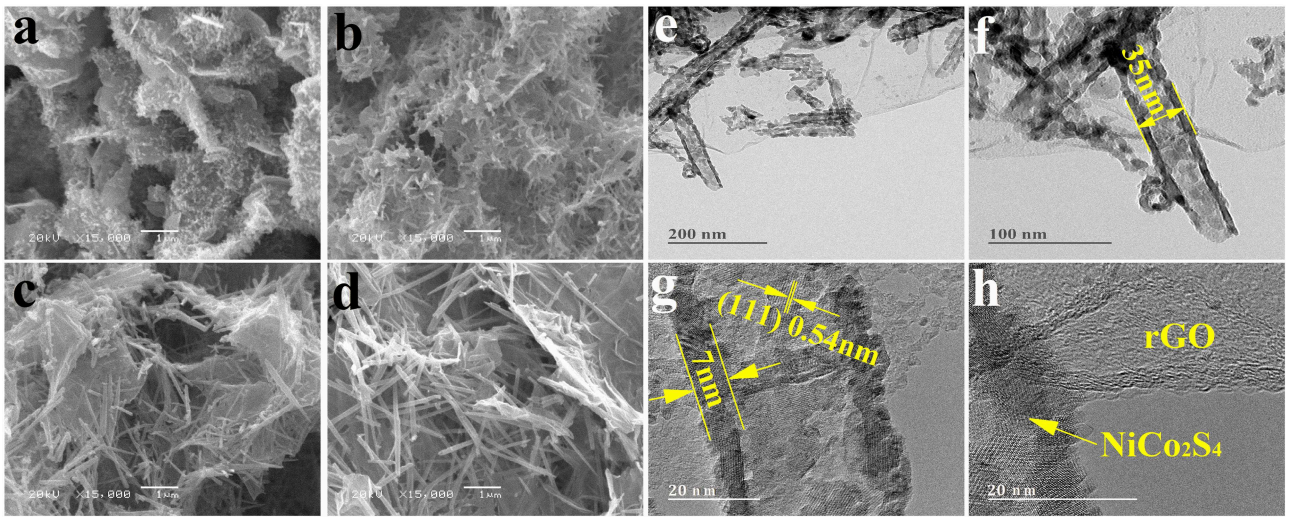

FIGURE 2 | The morphology of $Ni_xCo_yS_4$/rGO composites. **(a–d)** SEM images of $Ni_xCo_yS_4$/rGO composites; $Ni_{2.15}Co_{1.37}S_4$/rGO **(a)**, $Ni_{1.64}Co_{2.40}S_4$/rGO **(b)**, $Ni_{1.02}Co_{2.98}S_4$/rGO **(c)**, and $Ni_{0.60}Co_{3.60}S_4$/rGO **(d)**. **(e–h)** TEM and HRTEM images of $Ni_{1.64}Co_{2.40}S_4$/rGO; TEM images of $Ni_{1.64}Co_{2.40}S_4$/rGO **(e,f)**; HRTEM images of $Ni_{1.64}Co_{2.40}S_4$/rGO **(g,h)**.

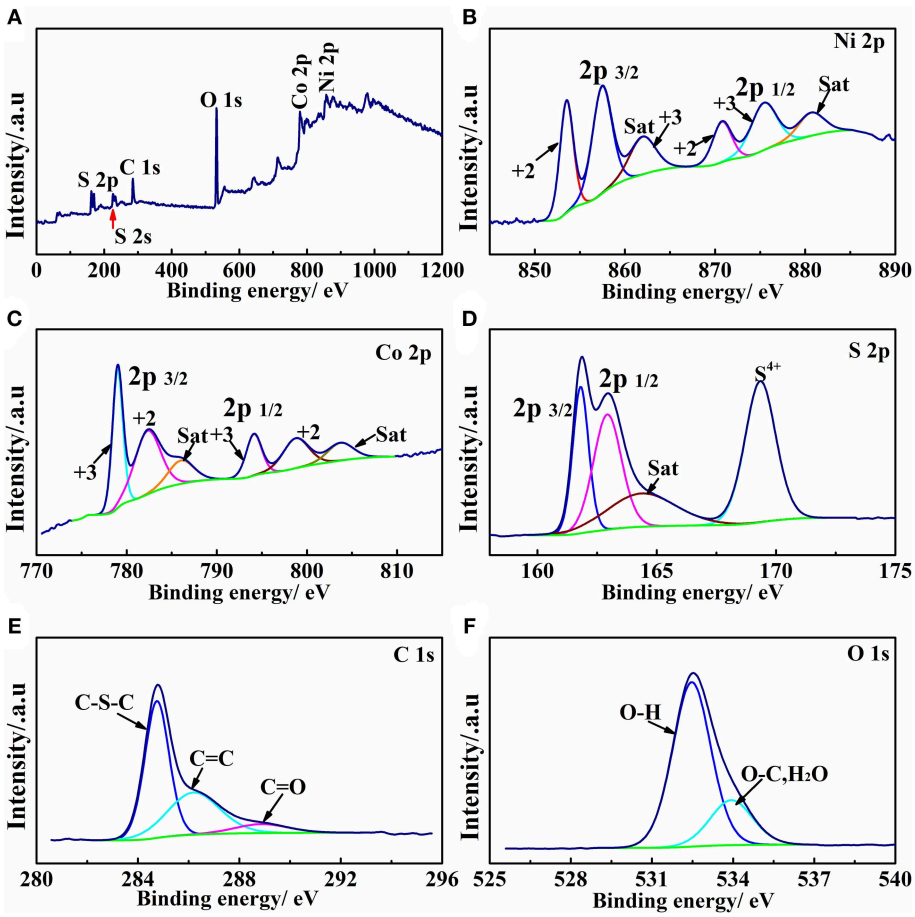

FIGURE 3 | XPS spectrum of $Ni_{1.64}Co_{2.40}S_4$/rGO composite: survey scan **(A)**, High-resolution spectra of Ni 2p **(B)**, Co 2p **(C)**, S 2p **(D)**, C 1s **(E),** and O 1s **(F)**, respectively.

(X-ray photoelectron spectroscopy) is utilized to analyze the elemental composition and valence state of the material. **Figure 3** shows survey, Ni 2p, Co 2p, S 2p, C 1s, and O 1s spectrum of the $Ni_{1.64}Co_{2.40}S_4$/rGO composite, and **Table S2** lists the peak fitting parameters of all spectrums. As shown in **Figure 3A**, it can be confirmed that Ni, Co, S, C, and O elements exist on the surface of $Ni_{1.64}Co_{2.40}S_4$/rGO composite. In high resolution spectrums of Ni 2p and Co 2p, the spectrums can be classified into 2p 3/2 and 2p 1/2 sections, and the corresponding satellite peaks are labeled as "Sat" in the plot. Specifically, the peaks at 853.5 and 870.8 eV in Ni 2p correspond to Ni^{2+}, and the peaks at 857.7 and 875.5 eV can be assigned to Ni^{3+}, confirming the coexistence of both Ni^{2+} and Ni^{3+} in the composite. Similarly, the peaks located at 779.0 eV, 794.1 eV in Co 2p corresponds to the Co^{3+}, and the peaks at 782.2 eV, 798.8 eV of Co 2p spectrums associates to the Co^{2+}, suggesting the coexistence of Co^{3+} and Co^{2+} in $Ni_{1.64}Co_{2.40}S_4$/rGO composite as well (Fan et al., 2017; Qin et al., 2017). For the S 2p spectrum, the peak located at 161.8 eV for S 2p 3/2 is attributed to S^{2-} or C-S-C bonds on the surface (Chen X. et al., 2014), while the peak at 162.9 eV for S 2p1/2 can be ascribed to S-M (metal) bonds. In addition, the peak at a high binding energy of 169.6 eV (satellite) can be attributed to the highly oxidized state sulfur species (S^{4+}) (Ma et al., 2016). The added $Na_2S{\cdot}9H_2O$ act as both of S^{2-} sources and reductant during the high temperature ion-exchange reaction, in which part of S^{2-} loses electrons and been oxidized to the higher-valence, and the GO been reduced to rGO simultaneously. Furthermore, the C 1s spectrum exhibits a major peak at 284.7 eV attributed to C-S-C bonds (Wenfang et al., 2015). Additionally, a peak located at 285.9 eV in the C 1s spectra corresponds to the C=C bond (aromatic-linked carbon), while the weak peak at 289.2 eV can be ascribed to the carboxyl groups (C=O) and sp^2 hybridized carbon from rGO, the low strength of the peak at 289.2 eV also indicates that the graphene has been reduced (Qin et al., 2017). The S 2p and C 1s XPS results reveal the existence of S-M (M=Ni or Co) and C-S-C bonds, respectively, which verifies the doping of S into rGO and the formation of transition metal sulfides in the composite material. Based on the XRD, SEM, TEM, and XPS results as analyzed in **Figures 1–3**, we proofed that the $Ni_xCo_yS_4$/rGO composites can be synthesized by such *in situ* growth—ion exchange strategy.

The electrochemical performances of $Ni_xCo_yS_4$/rGO composites are measured by cyclic voltammetry at various scan rates in a three-electrode cell as shown in **Figure 4**. For all composites, anodic and cathodic peaks with good symmetry indicate the good reversibility of the materials. The positions of anodic and cathodic peaks shift to the more positive and more negative directions with the increase of scan rates from 1 mV s^{-1} to 100 mV s^{-1}, which implies an increase of the polarization. It is known to all that the relationship between scan rate and current density is an effective method to distinguish capacitive contribution by the $i = av^b$ formula. Specifically, when the b value is 1/2, the electrode shows a total diffusion-limited behavior ($i = av^{1/2}$); and when the b value is 1, the electrode shows a capacitive process (Lim et al., 2015). **Figures 4E–H** show the b values of $Ni_{2.15}Co_{1.37}S_4$/rGO, $Ni_{1.64}Co_{2.40}S_4$/rGO, $Ni_{1.02}Co_{2.98}S_4$/rGO and $Ni_{0.60}Co_{3.60}S_4$/rGO as deduced from the slope of log (i)—log (v) curves, which are 0.55, 0.78, 0.86, and 0.89, respectively. The b values of the electrodes increase with the decrease of Ni/Co ratio, which implies that the $Ni_{2.15}Co_{1.37}S_4$/rGO composite is mainly diffusion-controlled kinetics behavior, and gradually transforms to the capacitive behavior for the $Ni_{0.60}Co_{3.60}S_4$/rGO composites. As the switch of kinetics behavior from diffusion-controlled to capacitive behavior, it will accelerate the charge transfer process so as to improve the rate capability of the $Ni_xCo_yS_4$/rGO composites.

The CV results of $Ni_{2.15}Co_{1.37}S_4$/rGO, $Ni_{1.64}Co_{2.40}S_4$/rGO, $Ni_{1.02}Co_{2.98}S_4$/rGO, and $Ni_{0.60}Co_{3.60}S_4$/rGO at 1 mV s^{-1} are presented in **Figure 5A**. Obviously, the $Ni_{2.15}Co_{1.37}S_4$/rGO material has the largest integral area, indicating the highest specific capacitance as compared to other samples. The specific capacitance of the material decreases with the decrease of Ni/Co ratio in $Ni_xCo_yS_4$/rGO composites, which is related to the microstructure transformation of the material. Specifically, $Ni_{1.64}Co_{2.40}S_4$/rGO consists of tiny one-dimensional nano-needles that convince to the sufficient contact between the active material and the electrolyte during the electrode process. In addition, the response current of the CV curves is a combination of capacitor and diffusion-controlled behavior. The respective contribution between diffusion-controlled and capacitive capacitance can be calculated by the following equation (Lim et al., 2015):

$$i(V) = k_1 v + k_2 v^{1/2} \quad (1)$$

The capacitance proportion of diffusion-controlled process and capacitor-like processes are expressed by $k_1 v$ and $k_2 v^{1/2}$, respectively. The capacitive-contribution of $Ni_{1.64}Co_{2.40}S_4$/rGO is 79.83% at 1 mV s^{-1} as shown in **Figure S7**, which confirms that the specific capacitance is mainly contributed by the capacitive-like process. Besides, the difference between the oxidation potential and reduction potential decrease obviously (the potential differences of $Ni_xCo_yS_4$/rGO composites are 0.132 V ($Ni_{2.15}Co_{1.37}S_4$/rGO), 0.104 V ($Ni_{1.64}Co_{2.40}S_4$/rGO), 0.089 V ($Ni_{1.02}Co_{2.98}S_4$/rGO), and 0.093 V ($Ni_{0.60}Co_{3.60}S_4$/rGO) respectively), indicating an gradually improved reversibility of the composites, which is beneficial to improve the rate performance of the electrodes. **Figures 5B,C** shows the rate capability of the composites as the current density range from 1 A g^{-1} to 20 A g^{-1}. It is noteworthy that the rate performance is improved distinctively with the decrease of Ni/Co molar ratio in composites. Specifically, when the current density increase to 20 A g^{-1}, the $Ni_{1.64}Co_{2.40}S_4$/rGO, $Ni_{1.02}Co_{2.98}S_4$/rGO, and $Ni_{0.60}Co_{3.60}S_4$/rGO composites can recover 92.6, 99.5, and 99.6% of their capacitance determined at 1 A g^{-1}, respectively (**Table S3**). In contrast, the $Ni_{2.15}Co_{1.37}S_4$/rGO composite can only retain 68.9% of its capacitance determined at 1 A g^{-1} under the same condition (**Table S3**). Our detailed electronic conductivity results (**Figure 5D**) evidence that higher Co content in $Ni_xCo_yS_4$/rGO composites is beneficial to improve the electronic conductivity of the composites, which is the main reason for the improvement of rate performance. Considering the merits of capacitance and rate capability of the composites, $Ni_{1.64}Co_{2.40}S_4$/rGO exhibits the best comprehensive performance in the application of supercapacitor, which delivers the capacitance of 1,089 F g^{-1} at the current density of 1 A g^{-1},

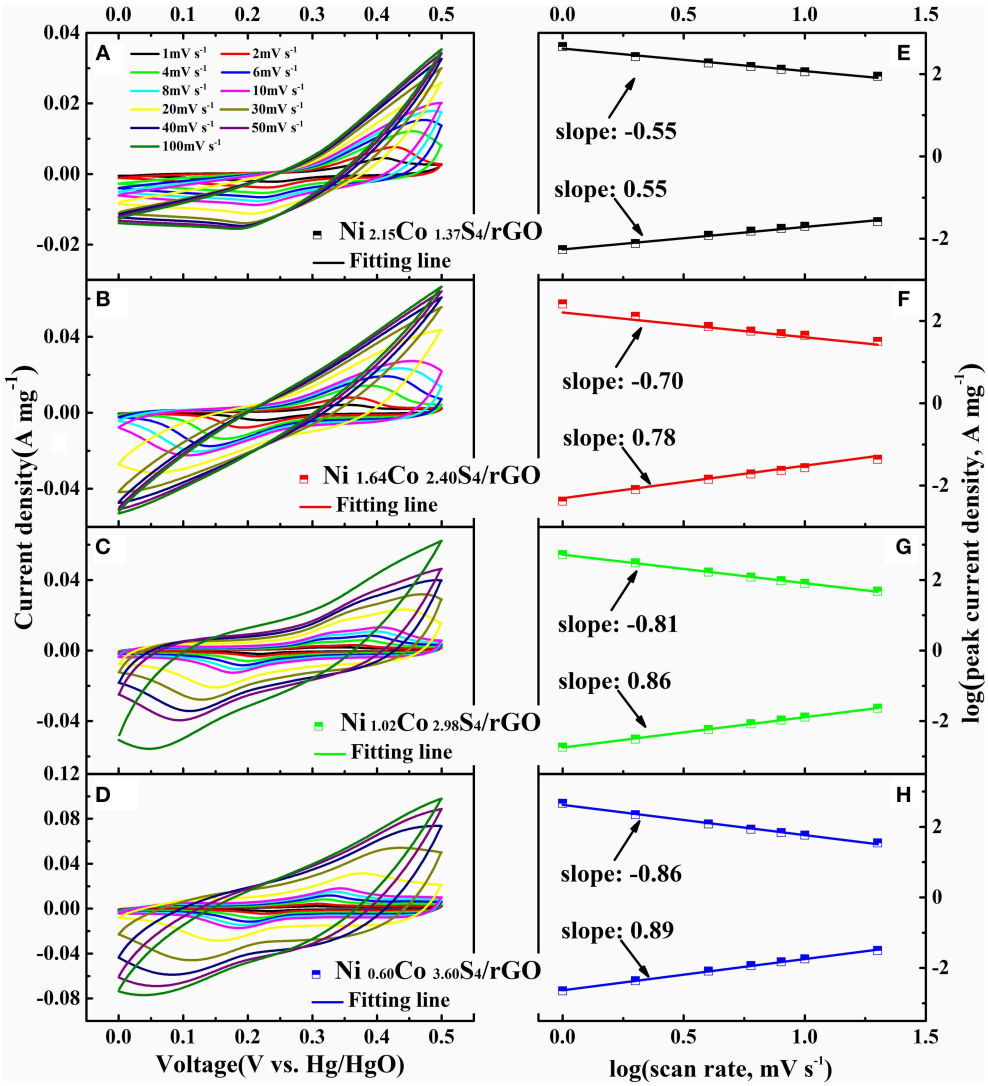

FIGURE 4 | Electrochemical properties of $Ni_xCo_yS_4$/rGO composites at three-electrode cells. CV curves of $Ni_{2.15}Co_{1.37}S_4$/rGO, $Ni_{1.64}Co_{2.40}S_4$/rGO, $Ni_{1.02}Co_{2.98}S_4$/rGO, and $Ni_{0.60}Co_{3.60}S_4$/rGO at different scan rates **(A–D)**; relationship between scan rate and current density of $Ni_{2.15}Co_{1.37}S_4$/rGO, $Ni_{1.64}Co_{2.40}S_4$/rGO, $Ni_{1.02}Co_{2.98}S_4$/rGO, and $Ni_{0.60}Co_{3.60}S_4$/rGO **(E–H)**.

and retains 1,008 F g^{-1} at the current density of 20 A g^{-1}. The GCD curves of $Ni_{2.15}Co_{1.37}S_4$/rGO, $Ni_{1.64}Co_{2.40}S_4$/rGO, $Ni_{1.02}Co_{2.98}S_4$/rGO, and $Ni_{0.60}Co_{3.60}S_4$/rGO at the current density of 1 A g^{-1} show nearly symmetric GCD curves, implying the high coulomb efficiency of the charge-discharge process (**Figure 5E** and **Figure S8**). Meanwhile, the time corresponding to the discharge platform gradually shortens with the decrease of Ni/Co ratio, indicating that the proportion of pseudocapacitance originated from Faraday reaction reduces. It is in well-accordance with the result of CV results as shown in **Figure 5A**. Moreover, the GCD curves of $Ni_{1.64}Co_{2.40}S_4$/rGO at various current densities in **Figure 5F** suggests that the electrode have excellent rate performance.

To demonstrate the practical application of $Ni_{1.64}Co_{2.40}S_4$/rGO composite for energy storage, an asymmetric supercapacitor marked as $Ni_{1.64}Co_{2.40}S_4$/rGO//AC was assembled, in which $Ni_{1.64}Co_{2.40}S_4$/rGO acts as the positive material and active carbon (AC) acts as the negative material. As shown in **Figure 6A**, the shape of the CV curve shows slight differences at various scan rate, indicating that the $Ni_{1.64}Co_{2.40}S_4$/rGO//AC asymmetric supercapacitor has good charge-discharge characteristics. The specific capacitances of $Ni_{1.64}Co_{2.40}S_4$/rGO//AC deduced from the integral area of CV curves at various current density are calculated and shown in **Figure 6B**. High capacitance (270.7 F g^{-1} at 1 mV s^{-1}) and high capacitance retention (68.5% at 100 mV s^{-1}) confirm the superior rate performance of the device, which is attributed to the proper composition and hollow structure of $Ni_{1.64}Co_{2.40}S_4$. The relationship between scan rate and current density of $Ni_{1.64}Co_{2.40}S_4$/rGO//AC during the charge-discharge process

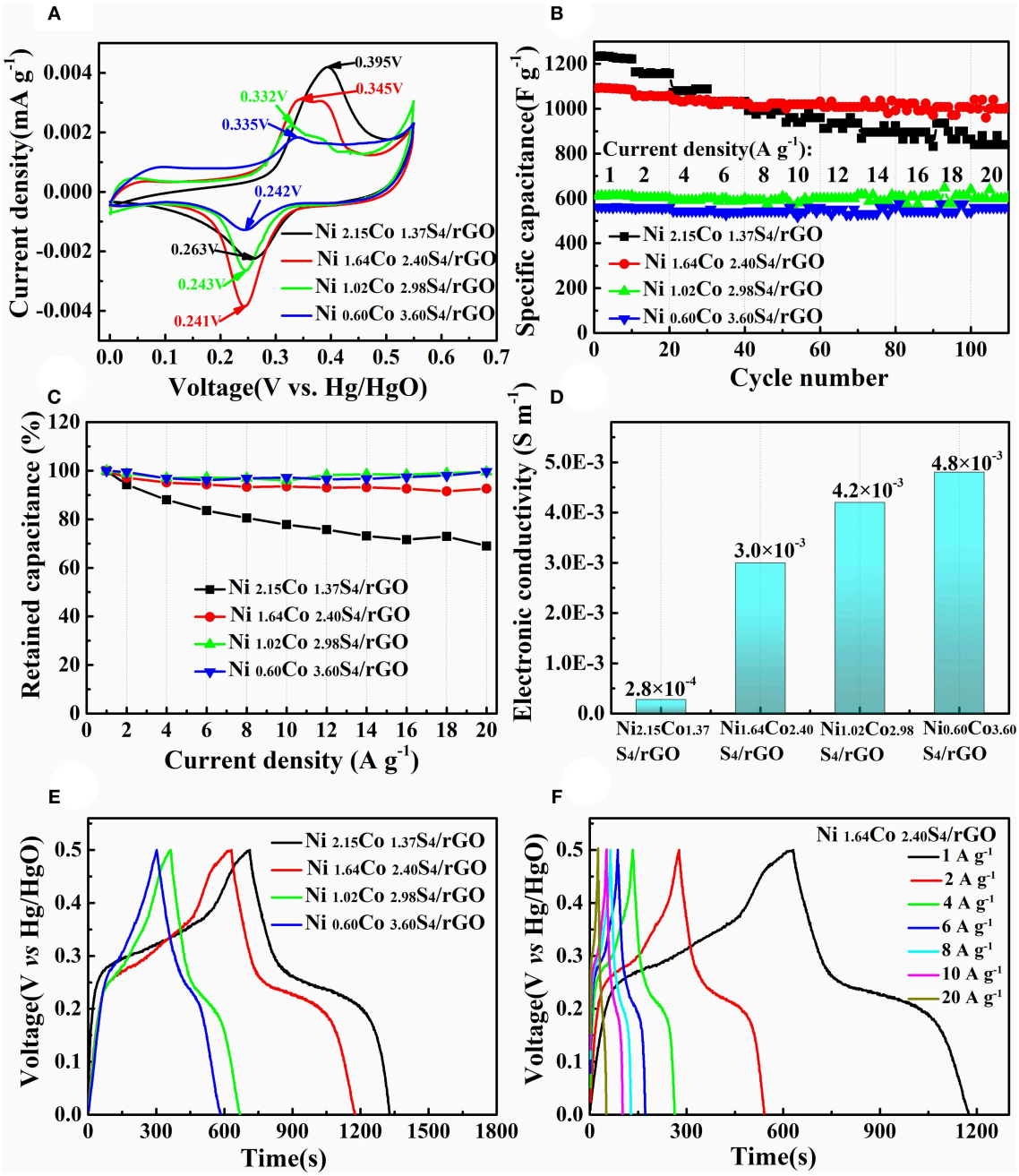

FIGURE 5 | CV curves of $Ni_xCo_yS_4$/rGO composites at the scan rate of 1 mV s^{-1} **(A)**; rate performance of $Ni_xCo_yS_4$/rGO composites at various current densities from 1 A g^{-1} to 20 A g^{-1} **(B)**; capacitance retention of $Ni_xCo_yS_4$/rGO composites with the increase of current density **(C)**; electronic conductivity of $Ni_xCo_yS_4$/rGO composites **(D)**; GCD curves of different composites at the current densities of 1 A g^{-1} **(E)**; GCD curves of $Ni_{1.64}Co_{2.40}S_4$/rGO at various current densities from 1 A g^{-1} to 20 A g^{-1} **(F)**.

is also calculated as shown in **Figure 6C**. The b value in the charge and discharge process are −0.70 and 0.77, respectively, which is quite consistent with the previous results as measured in the three-electrode cell. The specific capacitance and the corresponding GCD curves of the $Ni_{1.64}Co_{2.40}S_4$/rGO//AC asymmetric supercapacitor at various current densities are presented in **Figures 6D,E**, the specific capacitances are 265.5, 209.4, 195.6, 191.3, 180.0, and 168.8 F g^{-1} at the current density of 1, 10, 20, 30, 40, and 50 A g^{-1} respectively. The high capacitance retention of 63.6% at 50 A g^{-1} as compared to 1 A g^{-1} further verifies the excellent rate performance of the asymmetric supercapacitor. Furthermore, the long-term

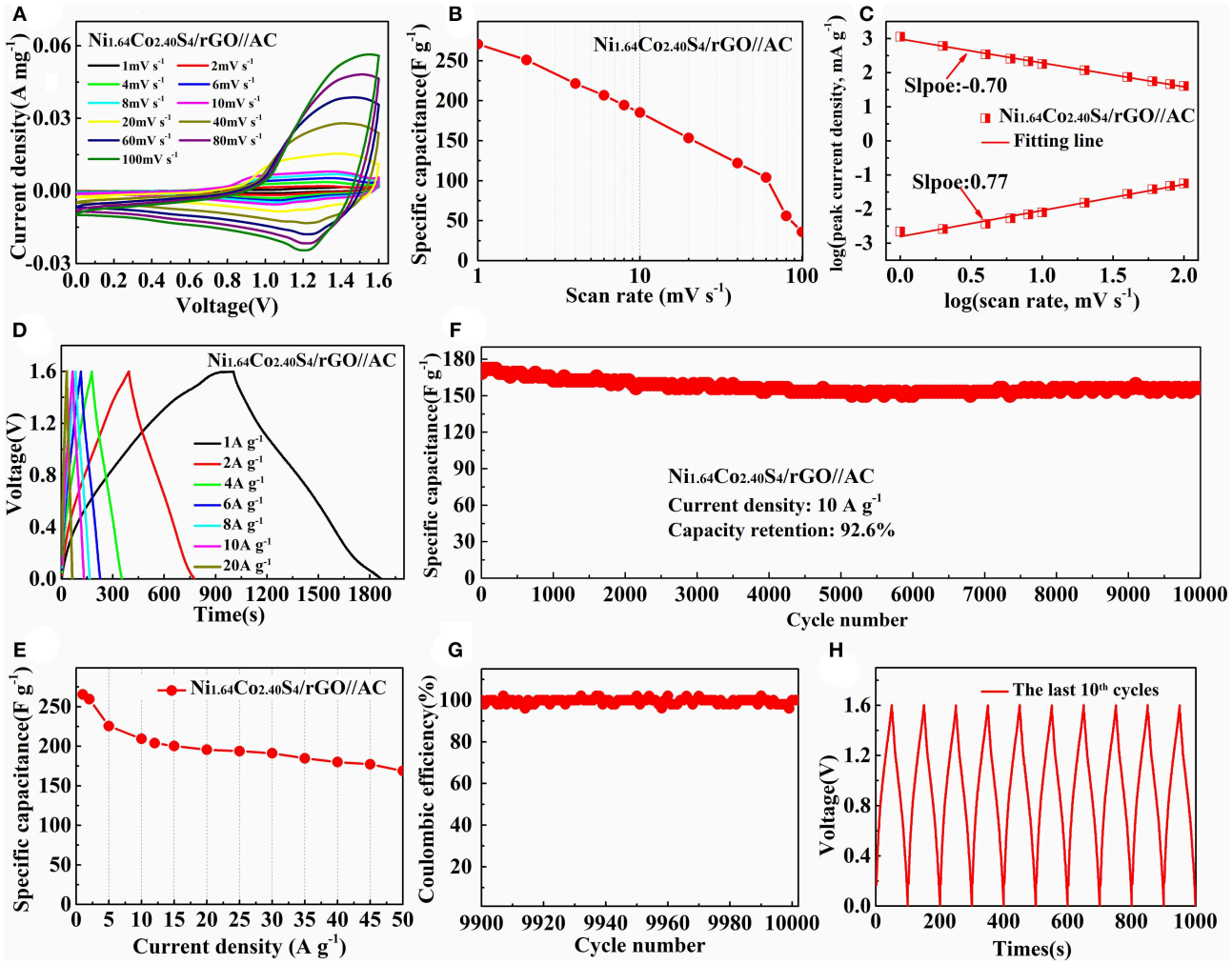

FIGURE 6 | Electrochemical properties of $Ni_{1.64}Co_{2.40}S_4$/rGO//AC asymmetric supercapacitor. CV curves of $Ni_{1.64}Co_{2.40}S_4$/rGO//AC at different scan rates **(A)**; specific capacitance of $Ni_{1.64}Co_{2.40}S_4$/rGO//AC calculated from CV curves **(B)**; relationship between scan rate and current density of $Ni_{1.64}Co_{2.40}S_4$/rGO//AC **(C)**; GCD curves of $Ni_{1.64}Co_{2.40}S_4$/rGO//AC at various current densities **(D)**; average specific capacitances in dependence of cycle number at various current densities from 1 A g^{-1} to 20 A g^{-1} **(E)**; cycle performance of $Ni_{1.64}Co_{2.40}S_4$/rGO//AC at the current density of 10 A g^{-1} **(F)**; columbic efficiency of $Ni_{1.64}Co_{2.40}S_4$/rGO//AC at the last 100 cycles **(G)**; GCD curves of $Ni_{1.64}Co_{2.40}S_4$/rGO//AC at the last 10 cycles of 10000 cycles **(H)**.

cycling measurements of the $Ni_{1.64}Co_{2.40}S_4$/rGO//AC at 10 A g^{-1} (as shown in **Figure 6F**) evidence the good cycling stability as it can retain 92.6 % of its initial capacitance after 10,000 times, demonstrating the high cyclic stability in terms of electrochemical and mechanical properties of the $Ni_{1.64}Co_{2.40}S_4$/rGO composites. Eventually, the high columbic efficiency approaching 100% and the symmetric GCD curves of the last few loops (**Figures 6G,H**) confirm the excellent electrochemical performance of the $Ni_{1.64}Co_{2.40}S_4$/rGO//AC asymmetric supercapacitor.

For positioning the level of as-obtained $Ni_{1.64}Co_{2.40}S_4$/rGO composite, we carefully investigated and compared the energy density and power density of supercapacitors using similar materials from the peer-reviewed papers. Ragone plot of these asymmetric supercapacitors derived from GCD tests are summarized and plotted in **Figure 7** and **Table S4**. Specifically, the $Ni_{1.64}Co_{2.40}S_4$/rGO//AC asymmetric supercapacitor can reach the maximum energy density of 47.2 Wh kg^{-1} at the power density of 200 W kg^{-1}, and retains an energy density of 30 Wh kg^{-1} even at high power density of 10 kW kg^{-1}. Impressively, the $Ni_{1.64}Co_{2.40}S_4$/rGO//AC asymmetric supercapacitor presented in this work is comparable or even superior to those of previous reported transition metal sulfides-based asymmetric supercapacitors and other supercapacitors (listed in **Table S5**), such as NCS/rGO/CNT-3//AC asymmetric supercapacitors (21.06 Wh kg^{-1} at the power density of 729 W kg^{-1} and 14.43 Wh kg^{-1} at the power density of 3646 W kg^{-1}) (Chiu and Chen, 2018), rGO/$CoNiS_x$/N–C//AC asymmetric supercapacitors (32.9 Wh kg^{-1} at the power density of 229.2 W kg^{-1} and 20.9 Wh kg^{-1} at the power density of 1833.3 W kg^{-1})

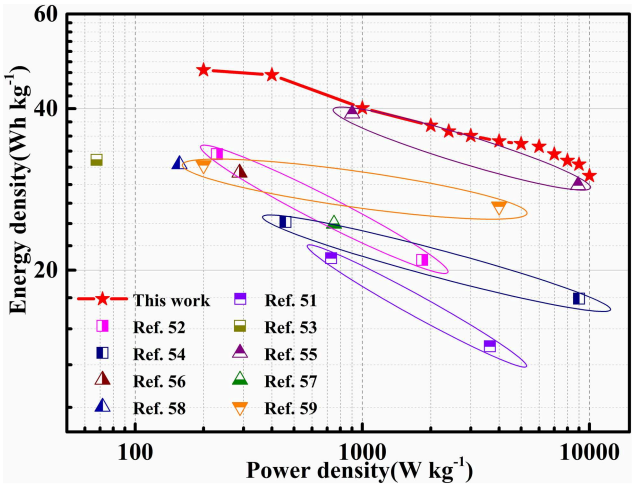

FIGURE 7 | Comparison of energy densities among as-constructed $Ni_{1.64}Co_{2.40}S_4$/rGO//AC with recently reported asymmetric supercapacitors.

(Chen Q. et al., 2018), $NiCo_2S_4$@CNFs//AC@pCNFs asymmetric supercapacitors (32.1 Wh kg^{-1} at the power density of 67.6 W kg^{-1} and 5.3 Wh kg^{-1} at the power density of 1,270 W kg^{-1}) (Liu et al., 2018b), GCM//H-GCS FASC (24.6 Wh kg^{-1} at the power density of 459.3 W kg^{-1} and 17.7 Wh kg^{-1} at the power density of 9005.3 W kg^{-1}) (Wu S. et al., 2018), NSC-900/MnO_2//NSC-900 asymmetric supercapacitors (39.15 Wh kg^{-1} at the power density of 901 W kg^{-1} and 28.8 Wh kg^{-1} at the power density of 8,907 W kg^{-1}) (Miao et al., 2018), $NiCo_2S_4$@NiO//AC (30.38 Wh kg^{-1} at the power density of 288 W kg^{-1}) (Huang et al., 2016), $NiCo_2S_4$/RGO//AC(24.4 Wh kg^{-1} at the power density of 750 W kg^{-1}) (Li Z. et al., 2016), $NiCo_2S_4$ nanotube arrays-Ni foam//RGO (31.5 Wh kg^{-1} at the power density of 156.6 W kg^{-1}) (Chen H. et al., 2014), Co_9S_8 nanoflake//AC (31.4 Wh kg^{-1} at the power density of 200 W kg^{-1} and 26.3 Wh kg^{-1} at the power density of 4,000 W kg^{-1}) (Rakhi et al., 2014).

CONCLUSION

We have reported an *in situ* growth—ion exchange method to synthesize $Ni_xCo_yS_4$/rGO composites with high energy and power density. We concluded from the composition, electronic conductivity, and electrochemical measurements that proper Ni/Co molar ratio in $Ni_xCo_yS_4$/rGO composites is vital to synthesize the material with high capacitance and rate capability. Here the as-prepared $Ni_{1.64}Co_{2.40}S_4$/rGO composite shows the best overall electrochemical performance among the obtained samples as it delivers a specific capacitance of 1,089 F g^{-1} at 1 A g^{-1}, and it maintains 1,008 F g^{-1} at high current density of 20 A g^{-1}. The derived $Ni_{1.64}Co_{2.40}S_4$/rGO//AC asymmetric supercapacitor offers high energy density of 47.2 Wh kg^{-1} (200 W kg^{-1}), together with a superior cyclic stability (maintaining 92.6 % of capacitance retention after 10,000 cycles at 10 A g^{-1}). Through this study, the synthesized and characterized $Ni_{1.64}Co_{2.40}S_4$/rGO composite provides a promising material for fabricating supercapacitors with both high energy and power density.

DATA AVAILABILITY

All datasets generated for this study are included in the manuscript/**Supplementary Files**.

AUTHOR CONTRIBUTIONS

The design and conduction of the experiment, the acquisition of data, the writing and modification of the paper are completed by MD. ZW and JW helped perfecting the experimental ideas and technical route. GY devoted many efforts to revise the manuscript. HG and XL gave advices during the discussion of the experimental results.

FUNDING

This research was supported by the National Science Foundation of China (51674295, 51804344), the Fundamental Research Funds for the Central University of Central South University (2018zzts017), the Hunan Provincial Innovation Foundation for Postgraduate (CX2018B088).

SUPPLEMENTARY MATERIAL

The Supplementary Material for this article can be found online at: https://www.frontiersin.org/articles/10.3389/fmats.2019.00176/full#supplementary-material

Supporting information for publication is available. XRD patterns, SEM images, TEM images of precursors; XPS, SEM, and EDS results of GO and rGO-$Na_2S{\cdot}9H_2O$; GCD curves of $Ni_{2.15}Co_{1.37}S_4$/rGO, $Ni_{1.02}Co_{2.98}S_4$/rGO, and $Ni_{0.60}Co_{3.60}S_4$/rGO; C-S and ICP results of $Ni_xCo_yS_4$/rGO composites.

REFERENCES

Annamalai, K. P., Liu, L., and Tao, Y. (2017). Highly exposed nickel cobalt sulfide–rGO nanoporous structures: an advanced energy-storage electrode material. *J. Mater. Chem. A* 5, 9991–9997. doi: 10.1039/C7TA01735A

Booth, T. J., Blake, P., Nair, R. R., Jiang, D., Hill, E. W., Bangert, U., et al. (2008). Macroscopic graphene membranes and their extraordinary stiffness. *Nano Lett.* 8, 2442–2446. doi: 10.1021/nl801412y

Brousse, T. (2015). To be or not to be pseudocapacitive? *J. Electrochem. Soc.* 162, A5185–A5189. doi: 10.1149/2.0201505jes

Chen, H., Jiang J., Zhang, L., Xia, D., Zhao, Y., Guo, D., et al. (2014). *In situ* growth of $NiCo_2S_4$ nanotube arrays on Ni foam for supercapacitors: maximizing utilization efficiency at high mass loading to achieve ultrahigh areal pseudocapacitance. *J. Power Sources* 254, 249–257. doi: 10.1016/j.jpowsour.2013.12.092

Chen, H., Jiang, J., Zhang, L., Wan, H., Qi, T., and Xia, D. (2013). Highly conductive $NiCo_2S_4$ urchin-like nanostructures for high-rate pseudocapacitors. *Nanoscale* 5, 8879–8883. doi: 10.1039/c3nr02958a

Chen, J., Li, L., Wu, L., Yao, Q., Yang, H., Liu, Z., et al. (2018). Enhanced cycle stability of $Na_{0.9}Ni_{0.45}Mn_{0.55}O_2$ through tailoring O_3/P_2

hybrid structures for sodium-ion batteries. *J. Power Sources* 406, 110–117. doi: 10.1016/j.jpowsour.2018.10.058

Chen, Q., Miao, J., Quan, L., Cai, D., and Zhan, H. (2018). Bimetallic $CoNiS_x$ nanocrystallites embedded in nitrogen-doped carbon anchored on reduced graphene oxide for high-performance supercapacitors. *Nanoscale* 10, 4051–4060. doi: 10.1039/C7NR08284C

Chen, X., Chen, X., Xu, X., Yang, Z., Liu, Z., Zhang, L., et al. (2014). Sulfur-doped porous reduced graphene oxide hollow nanosphere frameworks as metal-free electrocatalysts for oxygen reduction reaction and as supercapacitor electrode materials. *Nanoscale* 6, 13740–13747. doi: 10.1039/C4NR04783D

Chiu, C. T., and Chen, D. H. (2018). One-step hydrothermal synthesis of three-dimensional porous Ni-Co sulfide/reduced graphene oxide composite with optimal incorporation of carbon nanotubes for high performance supercapacitors. *Nanotechnology* 29:175602. doi: 10.1088/1361-6528/aaaff5

Deng, Y., Xu, A., Lu, W., Yu, Y., Fua, C., and Shua, T. (2017). Graphene-based ordered mesoporous carbon hybrids with large surface areas for supercapacitor. *New J. Chem.* 42, 7043–7048. doi: 10.1039/C7NJ03923A

Dong, M., Wang, Z., Li, X., Guo, H., and Wang, J. (2018). A smart architecture of nickel-cobalt sulfide nanotubes assembled nanoclusters for high-performance pseudocapacitor. *J. Alloys Compd.* 765, 505–511. doi: 10.1016/j.jallcom.2018.06.179

Eftekhari, A., Li, L., and Yang, Y. (2017). Polyaniline supercapacitors. *J. Power Sources* 347, 86–107. doi: 10.1016/j.jpowsour.2017.02.054

Fan, Y.-M., Liu, Y., Liu, X., Liu, Y., and Fan, L.-Z. (2017). Hierarchical porous $NiCo_2S_4$-rGO composites for high-performance supercapacitors. *Electrochim. Acta* 249, 1–8. doi: 10.1016/j.electacta.2017.07.175

Gao, Z., Chen, C., Chang, J., Chen, L., Wang, P., Wu, D., et al. (2018). Enhanced cycleability of faradic $CoNi_2S_4$ electrode by reduced graphene oxide coating for efficient asymmetric supercapacitor. *Electrochim. Acta* 281, 394–404. doi: 10.1016/j.electacta.2018.05.194

Gilshteyn, E. P., Amanbayev, D., Anisimov, A. S., Kallio, T., and Nasibulin, A. G. (2017). All-nanotube stretchable supercapacitor with low equivalent series resistance. *Sci. Rep.* 7:17449. doi: 10.1038/s41598-017-17801-4

Huang, Y., Shi, T., Jiang, S., Cheng, S., Tao, X., Zhong, Y., et al. (2016). Enhanced cycling stability of $NiCo_2S_4$@NiO core-shell nanowire arrays for all-solid-state asymmetric supercapacitors. *Sci. Rep.* 6:38620. doi: 10.1038/srep38620

Jiang, Y., and Liu, J. (2019). Definitions of pseudocapacitive materials: a brief review. *Energy Environ. Mater.* 2, 30–37. doi: 10.1002/eem2.12028

Jinlong, L., Tongxiang, L., Meng, Y., Ken, S., and Hideo, M. (2017). Performance comparison of $NiCo_2O_4$ and $NiCo_2S_4$ formed on Ni foam for supercapacitors. *Compos. Part B* 123, 28–33. doi: 10.1016/j.compositesb.2017.05.021

Ke, Q., and Wang, J. (2016). Graphene-based materials for supercapacitor electrodes – a review. *J. Materiom.* 2, 37–54. doi: 10.1016/j.jmat.2016.01.001

Lee, C., Wei, X., Kysar, J. W., and Hone, J. (2008). Measurement of the elastic properties and intrinsic strength of monolayer graphene. *Science* 321, 385–388. doi: 10.1126/science.1157996

Li, D., Gong, Y., and Pan, C. (2016). Facile synthesis of hybrid CNTs/$NiCo_2S_4$ composite for high performance supercapacitors. *Sci. Rep.* 6:29788. doi: 10.1038/srep29788

Li, L., Chen, Z., Zhang, Q., Xu, M., Zhou, X., Zhu, H., et al. (2015). A hydrolysis-hydrothermal route for the synthesis of ultrathin $LiAlO_2$-inlaid $LiNi_{0.5}Co_{0.2}Mn_{0.3}O_2$ as a high-performance cathode material for lithium ion batteries. *J. Mater. Chem. A* 3, 894–904. doi: 10.1039/C4TA05902F

Li, Z., Ji, X., Han, J., Hu, Y., and Guo, R. (2016). $NiCo_2S_4$ nanoparticles anchored on reduced graphene oxide sheets: *in-situ* synthesis and enhanced capacitive performance. *J. Colloid Interface Sci.* 477, 46–53. doi: 10.1016/j.jcis.2016.05.038

Liang, K., He, W., Deng, X., Ma, H., and Xu, X. (2018). Controlled synthesis of $NiCo_2S_4$ hollow spheres as high-performance electrode materials for supercapacitors. *J. Alloys Compd.* 735, 1395–1401. doi: 10.1016/j.jallcom.2017.11.153

Lim, E., Jo, C., Kim, H., Kim, M. H., Mun, Y., Chun, J., et al. (2015). Facile synthesis of Nb_2O_5@carbon core-shell nanocrystals with controlled crystalline structure for high-power anodes in hybrid supercapacitors. *ACS Nano* 9, 7497–7505. doi: 10.1021/acsnano.5b02601

Liu, S., Cai, Y., Zhao, X., Liang, Y., Zheng, M., Hu, H., et al. (2017). Sulfur-doped nanoporous carbon spheres with ultrahigh specific surface area and high electrochemical activity for supercapacitor. *J. Power Sources* 360, 373–382. doi: 10.1016/j.jpowsour.2017.06.029

Liu, Y., Fan, X., Huang, X., Liu, D., Dou, A., Su, M., et al. (2018a). Electrochemical performance of $Li_{1.2}Ni_{0.2}Mn_{0.6}O_2$ coated with a facilely synthesized $Li_{1.3}Al_{0.3}Ti_{1.7}(PO_4)_3$. *J. Power Sources* 403, 27–37. doi: 10.1016/j.jpowsour.2018.09.082

Liu, Y., Jiang, G., Sun, S., Xu, B., Zhou, J., Zhang, Y., et al. (2018b). Decoration of carbon nanofibers with $NiCo_2S_4$ nanoparticles for flexible asymmetric supercapacitors. *J. Alloys Compd.* 731, 560–568. doi: 10.1016/j.jallcom.2017.10.078

Liu, Y., Wang, Q., Zhang, Z., Dou, A., Pan, J., and Su, M. (2016). Investigation the electrochemical performance of layered cathode material $Li_{1.2}Ni_{0.2}Mn_{0.6}O_2$ coated with $Li_4Ti_5O_{12}$. *Adv. Powder Technol.* 27, 1481–1487. doi: 10.1016/j.apt.2016.05.008

Ma, L., Chen, T., Li, S., Gui, P., and Fang, G. (2019). A 3D self-supported coralline-like $CuCo_2S_4$@$NiCo_2S_4$ core-shell nanostructure composite for high-performance solid-state asymmetrical supercapacitors. *Nanotechnology* 30:255603. doi: 10.1088/1361-6528/ab08fb

Ma, L., Hu, Y., Chen, R., Zhu, G., Chen, T., Lv, H., et al. (2016). Self-assembled ultrathin $NiCo_2S_4$ nanoflakes grown on Ni foam as high-performance flexible electrodes for hydrogen evolution reaction in alkaline solution. *Nano Energy* 24, 139–147. doi: 10.1016/j.nanoen.2016.04.024

Miao, L., Zhu, D., Liu, M., Duan, H., Wang, Z., Lv, Y., et al. (2018). N, S Co-doped hierarchical porous carbon rods derived from protic salt: facile synthesis for high energy density supercapacitors. *Electrochim. Acta* 274, 378–388. doi: 10.1016/j.electacta.2018.04.100

Mohamed, S. G., Hussain, I., and Shim, J. J. (2018). One-step synthesis of hollow C-$NiCo_2S_4$ nanostructures for high-performance supercapacitor electrodes. *Nanoscale* 10, 6620–6628. doi: 10.1039/C7NR07338K

Nan, H., Han, J., Luo, Q., Yin, X., Zhou, Y., Yao, Z., et al. (2018). Economically synthesized $NiCo_2S_4$/reduced graphene oxide composite as efficient counter electrode in dye-sensitized solar cell. *Appl. Surf. Sci.* 437, 227–232. doi: 10.1016/j.apsusc.2017.12.175

Qin, H., Yang, S., Zhao, W., Yang, Z., Li, X., Li, H., et al. (2017). Synthesis of mesoporous $NiCo_2S_4$ deposited on reduced graphite oxide assistant by co-polymer Pluronic F127 for high-performance supercapacitor. *Appl. Surf. Sci.* 420, 77–82. doi: 10.1016/j.apsusc.2017.05.048

Qu, C., Zhang, L., Meng, W., Liang, Z., Zhu, B., Dang, D., et al. (2018). MOF-derived α-NiS nanorods on graphene as an electrode for high-energy-density supercapacitors. *J. Mater. Chem. A* 6, 4003–4012. doi,: 10.1039/C.7T. A.11100B.

Rakhi, R. B., Alhebshi, N. A., Anjum, D. H., and Alshareef H. N. (2014). Nanostructured cobalt sulfide-on-fiber with tunable morphology as electrodes for asymmetric hybrid supercapacitors. *J. Mater. Chem. A* 9, 16190–16198. doi: 10.1039/C4TA03341H

Saha, S., Samanta, P., Murmu, N. C., and Kuila, T. (2018). A review on the heterostructure nanomaterials for supercapacitor application. *J. Energy Storage* 17, 181–202. doi: 10.1016/j.est.2018.03.006

Sarkar, A., Bera, S., and Chakraborty, A. K. (2018). $NiCo_2S_4$ nanorod embedded rGO sheets as electrodes for supercapacitor. *AIP Conf. Proc.* 1942:140029. doi: 10.1063/1.5029160

Simon, P., Gogotsi, Y., and Dunn, B. (2014). Where do batteries end and supercapacitors begin? *Mater. Sci.* 343, 1210–1211. doi: 10.1126/science.1249625

Tan, L., Li, X., Wang, Z., Guo, H., and Wang, J. (2018). Lightweight reduced graphene oxide@MoS_2 interlayer as polysulfide barrier for high-performance lithium-sulfur batteries. *ACS Appl. Mater. Interfaces* 10, 3707–3713. doi: 10.1021/acsami.7b18645

Wan, H., Jiang, J., Yu, J., Xu, K., Ling, M., Li, Z., et al. (2013). $NiCo_2S_4$ porous nanotubes synthesis via sacrificial templates: high-performance electrode materials of supercapacitors. *CrystEngComm* 15, 7649–7651. doi: 10.1039/c3ce41243a

Wang, H., Liang, M., Ma, C., Shi, W., Duan, D., He, G., et al. (2019). Novel dealloying-fabricated $NiCo_2S_4$ nanoparticles with excellent cycling performance for supercapacitors. *Nanotechnology* 30:235402. doi: 10.1088/1361-6528/ab0605

Wang, J., Zhang, G., Liu, Z., Li, H., Liu, Y., Wang, Z., et al. (2018). $Li_3V(MoO_4)_3$ as a novel electrode material with good lithium storage properties and improved initial coulombic efficiency. *Nano Energy* 44, 272–278. doi: 10.1016/j.nanoen.2017.11.079

Wang, Y., Yang, L., Liu, Y., Zhao, Q., Ding, F., Zou, P., et al. (2018). Colorimetric determination of dopamine by exploiting the enhanced oxidase mimicking activity of hierarchical $NiCo_2S_4$-rGO composites. *Mikrochim. Acta* 185, 496. doi: 10.1007/s00604-018-3035-8

Wen, Y., Peng, S., Wang, Z., Hao, J., Qin, T., Lu, S., et al. (2017). Facile synthesis of ultrathin $NiCo_2S_4$ nano-petals inspired by blooming buds for high-performance supercapacitors. *J. Mater. Chem. A* 5, 7144–7152. doi: 10.1039/C7TA01326D

Wenfang, D., Zhang, Y., Yang, L., Tan, Y., Ma, M., and Xie, Q. (2015). Sulfur-doped porous carbon nanosheets as an advanced electrode material for supercapacitors. *RSC Adv.* 5, 13046–13051. doi: 10.1039/C4RA14820G

Wu, F., Chen, S., Srot, V., Huang, Y., Sinha, S. K., Van Aken, P. A., et al. (2018). A sulfur-limonene-based electrode for lithium-sulfur batteries: high-performance by self-protection. *Adv. Mater.* 30:e1706643. doi: 10.1002/adma.201706643

Wu, S., Hui, K. S., and Hui, K. N. (2018). Carbon nanotube@manganese oxide nanosheet core-shell structure encapsulated within reduced graphene oxide film for flexible all-solid-state asymmetric supercapacitors. *Carbon N. Y.* 132, 776–784. doi: 10.1016/j.carbon.2017.12.051

Xiao, J., and Yang, S. (2011). Sequential crystallization of sea urchin-like bimetallic (Ni, Co) carbonate hydroxide and its morphology conserved conversion to porous $NiCo_2O_4$ spinel for pseudocapacitors. *RSC Adv.* 1:588. doi: 10.1039/c1ra00342a

Xiong, X., Waller, G., Ding, D., Chen, D., Rainwater, B., Zhao, B., et al. (2015). Controlled synthesis of $NiCo_2S_4$ nanostructured arrays on carbon fiber paper for high-performance pseudocapacitors. *Nano Energy* 16, 71–80. doi: 10.1016/j.nanoen.2015.06.018

Yan, G., Dugas, R., and Tarascon, J.-M. (2018). The $Na_3V_2(PO_4)_2$ F-3/carbon na-ion battery: its performance understanding as deduced from differential voltage analysis. *J. Electrochem. Soc.* 165, A220–A227. doi: 10.1149/2.0831802jes

Yuan, D., Huang, G., Yin, D., Wang, X., Wang, C., and Wang, L. (2017). Metal-organic framework template synthesis of $NiCo_2S_4$@C encapsulated in hollow nitrogen-doped carbon cubes with enhanced electrochemical performance for lithium storage. *ACS Appl. Mater. Interfaces* 9, 18178–18186. doi: 10.1021/acsami.7b02176

Zhang, L., Hu, X., Wang, Z., Sun, F., and Dorrell, D. G. (2018). A review of supercapacitor modeling, estimation, and applications: a control/management perspective. *Renew. Sustain. Energy Rev.* 81, 1868–1878. doi: 10.1016/j.rser.2017.05.283

Zhang, Q., Chen, H., Luo, L., Zhao, B., Luo, H., Han, X., et al. (2018). Harnessing the concurrent reaction dynamics in active Si and Ge to achieve high performance lithium-ion batteries. *Energy Environ. Sci.* 11, 669–681. doi: 10.1039/C8EE00239H

Zhao, F., Huang, W., Shi, Q., Zhou, D., Zhao, L., and Zhang, H. (2017). Low temperature fabrication of hydrangea-like $NiCo_2S_4$ as electrode materials for high performance supercapacitors. *Mater. Lett.* 186, 206–209. doi: 10.1016/j.matlet.2016.09.110

Zhong, S., Hong, W., Zhang, X., Liu, J., Li, Y., Shi, Y., et al. (2017). Synthesis of $xLiVPO_4F$ center dot $yLi_3V_2(PO_4)_3$/C composite as a potential cathode material for Li-ion batteries. *Ionics (Kiel).* 23, 813–819. doi: 10.1007/s11581-016-1875-y

Zhong, S., Wu, L., Zheng, J., and Liu, J. (2012). Preparation of high tap-density $9LiFePO_4$ center dot Li3V2(PO4)(3)/C composite cathode material by spray drying and post-calcining method. *Powder Technol.* 219, 45–48. doi: 10.1016/j.powtec.2011.12.005

Zhu, Y., Wu, Z., Jing, M., Yang, X., Song, W., and Ji, X. (2015). Mesoporous $NiCo_2S_4$ nanoparticles as high-performance electrode materials for supercapacitors. *J. Power Sources* 273, 584–590. doi: 10.1016/j.jpowsour.2014.09.144

Conflict of Interest Statement: The authors declare that the research was conducted in the absence of any commercial or financial relationships that could be construed as a potential conflict of interest.